

High-energy transmission Laue micro-beam X-ray diffraction: a probe for intra-granular lattice orientation and elastic strain in thicker samples

Felix Hofmann,^{a,b*} Xu Song,^b Brian Abbey,^c Tea-Sung Jun^d and Alexander M. Korsunsky^b

^aChemistry Department, Massachusetts Institute of Technology, 77 Massachusetts Avenue, Cambridge, MA 02139-4307, USA, ^bDepartment of Engineering Science, University of Oxford, Parks Road, Oxford, OX1 3PJ, UK, ^cARC Centre of Excellence for Coherent X-ray Science, School of Physics, Melbourne University, Melbourne, Australia, and ^dPOSCO Research Center, Nam-Gu, Pohang-Si, Gyeongsangbuk-do, 790-360, Korea. E-mail: felix.hofmann@trinity.oxon.org

An understanding of the mechanical response of modern engineering alloys to complex loading conditions is essential for the design of load-bearing components in high-performance safety-critical aerospace applications. A detailed knowledge of how material behaviour is modified by fatigue and the ability to predict failure reliably are vital for enhanced component performance. Unlike macroscopic bulk properties (*e.g.* stiffness, yield stress, *etc.*) that depend on the average behaviour of many grains, material failure is governed by 'weakest link'-type mechanisms. It is strongly dependent on the anisotropic single-crystal elastic-plastic behaviour, local morphology and microstructure, and grain-to-grain interactions. For the development and validation of models that capture these complex phenomena, the ability to probe deformation behaviour at the micro-scale is key. The diffraction of highly penetrating synchrotron X-rays is well suited to this purpose and micro-beam Laue diffraction is a particularly powerful tool that has emerged in recent years. Typically it uses photon energies of 5–25 keV, limiting penetration into the material, so that only thin samples or near-surface regions can be studied. In this paper the development of high-energy transmission Laue (HETL) micro-beam X-ray diffraction is described, extending the micro-beam Laue technique to significantly higher photon energies (50–150 keV). It allows the probing of thicker sample sections, with the potential for grain-level characterization of real engineering components. The new HETL technique is used to study the deformation behaviour of individual grains in a large-grained polycrystalline nickel sample during *in situ* tensile loading. Refinement of the Laue diffraction patterns yields lattice orientations and qualitative information about elastic strains. After deformation, bands of high lattice misorientation can be identified in the sample. Orientation spread within individual scattering volumes is studied using a pattern-matching approach. The results highlight the inability of a simple Schmid-factor model to capture the behaviour of individual grains and illustrate the need for complementary mechanical modelling.

1. Introduction

Classical material models aim to capture and predict the mechanical behaviour of ductile polycrystalline metallic aggregates used in structural engineering components at the macroscopic scale. They rely on the use of homogenized descriptions of the material's response, derived from macro-

scopic mechanical tests or by considering representative volume elements (RVEs). The mechanical behaviour is captured by a set of empirical constitutive equations that implicitly take into account a homogenized form of the details of behaviour at the finer underlying scales (Crisfield, 1991; Lemaitre *et al.*, 1994; Dunne & Petrinic, 2005). While this approach has served engineers well for over a hundred years,

it is now clear that, particularly in high-performance safety-critical applications, it is somewhat lacking. When operating a material close to its performance envelope, it is vital that the details of behaviour right down to the nano-scale are explicitly taken into account. This is particularly true since material strength and failure are governed by weakest-link-type mechanisms (*e.g.* fatigue, crack growth, damage) rather than average bulk properties (*e.g.* stiffness). In ductile metals the nucleation, interaction and self-organization of lattice defects, such as dislocations, vacancies and grain boundaries, are of key importance. Understanding, modelling, predicting and controlling the mechanical behaviour of polycrystalline aggregates is a complex multi-scale problem which requires a joined-up appreciation of processes across all structural scales.

The importance of size effects was first reported in the context of grain size strengthening in metals (Hall, 1951; Petch, 1953). Strain gradients play a key role, as highlighted by micro-indentation (McElhane *et al.*, 1998) or the deformation behaviour of metal matrix composites (Lloyd, 1994). In polycrystalline metallic aggregates they arise primarily due to the incompatibilities associated with the inhomogeneous elastic–plastic behaviour of neighbouring grains and the need to accommodate lattice rotations. Ashby (1970) first pointed out the fundamental difference between homogeneous plastic deformation that can be accommodated by an arbitrary distribution of statistically stored dislocations (SSDs) and the particular distributions of geometrically necessary dislocations (GNDs) required to accommodate plastic strain gradients.

To take into account explicitly the effects of GNDs, strain gradient crystal plasticity theories have been proposed (Aifantis, 1987; Fleck *et al.*, 1994; Fleck & Hutchinson, 2001). In these models the introduction of GNDs, in addition to the inherently random SSDs, results in increased strengthening of the material. In more recently proposed physically based formulations, the effects of strain gradients are directly introduced into the evolution laws of the internal slip systems (Busso *et al.*, 2000; Beaudoin *et al.*, 2000; Arsenlis & Parks, 2002). These models have been shown capable of providing great physical insight into the effects of microstructure on macroscopically observed phenomena, such as rate-independent plastic deformation and visco-plasticity in single- and polycrystalline materials (Meissonnier *et al.*, 2001; Cheong *et al.*, 2005).

The slip laws used in crystal plasticity simulations implicitly take into account a homogenized version of the finer details of single-crystal deformation by dislocation motion, interaction and propagation. Several different approaches have been proposed to study the collective behaviour of dislocations, from the very popular two-dimensional dislocation dynamics simulations based on the Van der Giessen and Needleman framework (Van der Giessen & Needleman, 1995; Deshpande *et al.*, 2003) to the physically more representative though computationally expensive three-dimensional simulations by Arsenlis, Bulatov, Cai *et al.* (Bulatov & Cai, 2006; Arsenlis *et al.*, 2007). Of course, the constitutive laws governing dislocation nucleation, motion and interaction are in turn an attempt

to capture the behaviour at the atomistic scale as defects move through the lattice (Bulatov *et al.*, 2006).

For further development and validation of material models, they must be complemented by experimental measurements at the same structural scale. For crystal plasticity models this comparison is often made at the macroscopic scale, averaging both numerically and experimentally over a large number of grains and neglecting the details of deformation at the micro-scale (Gloaguen *et al.*, 2007; Song *et al.*, 2008*a,b*). It has only fairly recently become possible to make a direct comparison of experiments and simulations at the grain level (Dunne *et al.*, 2007). Scanning electron microscopy combined with high-resolution electron backscatter diffraction (EBSD) (Wilkinson *et al.*, 2006*a,b*) as well as transmission electron microscopy are very valuable tools for this. However, their limitation to studies of the sample surface or very thin sections makes them unsuitable for non-destructive three-dimensional characterization of microstructure, orientation, stress and strain.

An alternative is provided by the diffraction of highly penetrating synchrotron X-rays. The micro-beam Laue technique is particularly well suited to the study of deformation in individual grains of polycrystalline aggregates. A focused polychromatic X-ray beam probe is used to illuminate a sampling volume smaller than the local grain size. The resulting single-crystal Laue diffraction patterns consisting of a number of Laue spots are recorded on an area detector. From indexation of the spots and refinement of their position, lattice orientation and deviatoric elastic strain in the illuminated volume can be deduced. The shape of individual Laue spots provides information about the orientation spread in the scattering volume. This can be interpreted in terms of the underlying dislocation arrangement and active slip system(s) based on knowledge of the lattice orientation changes induced by different GND populations (Barabash *et al.*, 2001, 2003, 2005). By rastering the micro-beam probe over the sample, maps of lattice orientation, strain, stress, active slip system, *etc.* can be built up.

Most micro-beam Laue experiments use a reflection geometry with the sample surface inclined at $\sim 45^\circ$ to the incident beam and an area detector positioned vertically above the sample at $2\theta = 90^\circ$ (angle between the incident beam and the vector from the sample to the detector centre). The range of photon energies available depends on the instrument, with a lower bound of 5–10 keV and an upper bound of 22–35 keV (Budai *et al.*, 2003; Yan & Noyan, 2005; Hofmann *et al.*, 2009). This widely accepted configuration is available at a number of beamlines around the world [*e.g.* BM32 (ESRF), Vespers (CLS), 34IDE (APS), 12.3.2 (ALS)] and has been applied to the study of a wide range of systems, such as thin films (Tamura *et al.*, 2003; Spolenak *et al.*, 2003), tin whiskers (Choi *et al.*, 2003), electro-migration (Barabash *et al.*, 2004*b*), *in situ* deformation of micro-pillars (Maass *et al.*, 2008*a,b*), *etc.*

Spatial resolution perpendicular to the incident X-ray beam is determined by the focal spot size. Sub-micrometre spot sizes can be routinely achieved using achromatic Kirkpatrick–Baez

(KB) focusing mirrors. The current record for the smallest focus of a polychromatic beam that has been demonstrated using KB mirrors currently stands at 7 nm (Mimura *et al.*, 2010). Spatial resolution along the axis of the incident beam is much more challenging to achieve. Samples with thickness of the order of the attenuation length or smaller are effectively self-collimating, in that the sampling volume length is defined by the sample thickness. The scattering volume length in bulk samples, on the other hand, is defined by the exponential drop-off in intensity due to absorption. Signal from deeply buried regions is limited by the noise floor.

To achieve spatial resolution along the incident beam direction comparable with the focal spot size, the differential aperture X-ray microscopy (DAXM) method can be used (Yang *et al.*, 2004; Larson *et al.*, 2004). Here, a knife-edge scan across the diffracted beams is performed with a tungsten wire. By considering intensity changes as a function of wire position and using ray tracing, the exact depth of origin of each scattered contribution collected on the detector can be determined and depth-resolved Laue patterns generated. A wide range of samples have been studied by DAXM, such as metal matrix composites (Bei *et al.*, 2008) or tin whiskers (Ice *et al.*, 2005), and its ability to provide depth-resolved information about elastic strain variation has been demonstrated (Larson *et al.*, 2002).

Alternative monochromatic beam techniques that can provide similar information are 3DXRD (Poulsen *et al.*, 2001; Nielsen *et al.*, 2001; Fu *et al.*, 2003) and diffraction contrast tomography (DCT) (Ludwig *et al.*, 2008, 2009; Johnson *et al.*, 2008). By applying tomographic reconstruction principles to grain-specific diffraction contrast and grain diffraction peak-shape, they allow non-destructive three-dimensional micro-structure mapping and give information about average elastic strain in each grain. Compared with DAXM, data acquisition is more rapid, making the mapping of large volumes feasible (King *et al.*, 2008, 2010). However, the use of diffraction contrast and topographical information puts a bound of a few tenths of a degree on the largest intra-granular misorientations that can be tolerated. In engineering samples, even very modest plastic deformation leads to intra-granular lattice misorientations beyond this threshold. DAXM has the demonstrated ability of resolving substantial lattice distortions and steep lattice rotations gradients, such as those introduced by friction stir processing (Barabash *et al.*, 2007). It also provides intra-granular resolution of strain and lattice orientation, which is a challenge by either DCT or 3DXRD, and does not require sample rotation. This makes it a very attractive tool for the study of grain-deformation mechanics at high spatial resolution and for the comparison with crystal plasticity and dislocation dynamics simulations.

The use of micro-beam Laue diffraction and DAXM for the study of grains embedded deep in the bulk of real engineering components is limited by absorption of the probing beam. Consider the example of nickel: in its commercially pure (cp) form it serves as a model of a ductile face-centred cubic (FCC) metal. In alloyed form it is central to high-temperature nickel-base superalloys (*e.g.* IN718 or Nimonic) used in power

generation and propulsion, and, with other alloying elements (Al, V, Cr, Fe, Ti), forms a variety of phases and structures, such as hard intermetallic precipitates (Ni₃Al); shape memory alloys (Ni–Ti); corrosion-resistant alloys (*e.g.* NiCrAlY), *etc.* In the classical low-energy micro-beam Laue diffraction configuration the attenuation length in nickel at 20 keV is 35.5 μm , limiting studies to the top $\sim 70 \mu\text{m}$ of near-surface material. For engineering components with several millimetres thicknesses this is not sufficient, considering for example welded components with complex defect and re-crystallization distribution through thickness. Penetration of the incident X-ray beam into the material can be enhanced by increasing the photon energies. This approach is commonly used in the powder diffraction community for monochromatic (Wanner & Dunand, 2000; Cheng *et al.*, 2009) and energy-dispersive (Korsunsky *et al.*, 2002, 2010; Steuwer *et al.*, 2005) high-energy X-ray measurements of lattice strains and texture. As the photon energy of the incident X-ray beam is increased, Bragg law dictates that the stronger lower-order reflections are forward scattered. This makes transmission geometry the natural choice. We recently reported first results from the extension of the micro-beam Laue technique to significantly higher photon energies (50 to 150 keV) (Hofmann *et al.*, 2010). As the attenuation length in nickel at a photon energy of 100 keV is $\sim 2.5 \text{ mm}$, this set-up makes the study of several-millimetre-thick sample sections feasible.

In this paper we describe in detail the application of high-energy transmission Laue (HETL) micro-beam X-ray diffraction to the study of intra-granular deformation behaviour of a polycrystalline large-grained nickel sample during *in situ* tensile loading. Initially, a detailed overview of the new experimental technique will be provided. Then we will focus on the evolution of lattice orientation with increasing loading and the information about grain-level deformation behaviour it provides. Finally, some avenues for future developments will be discussed and conclusions drawn.

2. Experimental set-up and sample

The experimental HETL configuration was developed at the high-energy beamline ID15 at the European Synchrotron Radiation Facility (ESRF). Two insertion devices are available on this beamline; a seven-pole 1.84 T asymmetric multipole wiggler (AMPW) and an in-vacuum undulator (U22). The AMPW is the more suitable source, providing a smooth photon energy spectrum with a critical energy of 44 keV and photon flux up to energies in excess of 600 keV. The incident beam was collimated to a size of $25 \mu\text{m} \times 25 \mu\text{m}$ by a set of precision slits. Downstream of the slits a fast shutter was mounted to allow accurate definition of exposure times. Just upstream of the sample an anti-scatter guard was placed to remove scatter from the collimating slits. Samples were mounted in a purpose-built tensile testing rig to allow the application of *in situ* loading (Fig. 1). To minimize experimental errors, accurate alignment of the tensile rig is vital such that the sample position along the beam direction does not change as the sample is translated horizontally or vertically. At

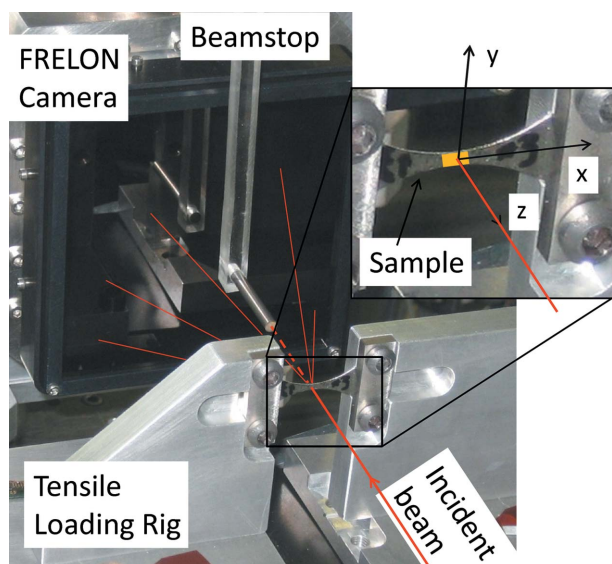


Figure 1 Image of the sample and detector arrangement for HETL measurements on ID15 (ESRF). Inset: close-up view of the sample and the laboratory coordinate axes.

106.7 mm downstream of the sample a scintillator of side length 96.64 mm, coupled to a FReLoN camera by a fibre optic taper, was positioned in transmission geometry. The angular acceptance was up to $2\theta \simeq 32^\circ$, covering the angular range in which reflections of sufficient brightness are expected. A tungsten rod was mounted close to the detector as a direct beamstop (Fig. 1).

Accurate calibration is vital for the analysis of Laue diffraction patterns. Spatial distortions are a common feature of X-ray area detectors using a scintillator coupled to a CCD by tapered optics. They arise due to imperfections of the optical taper which cause non-linear mapping of positions on the scintillator to positions on the CCD. In the FReLoN camera the largest deviation was ~ 20 pixels from the nominal position. To correct for these distortions, an absorbing mask with circular apertures of 0.75 mm diameter precisely positioned in a regular array with 2.5 mm spacing was used as a reference. The mask was placed directly in front of the scintillator and illuminated by a point source 1.5 m upstream of the detector. A fourth-order polynomial was then applied to re-map the recorded aperture positions in images of the mask to their nominal positions. The same distortion correction was applied to all experimentally recorded Laue patterns.

Calibration of the experimental geometry was based on Laue patterns from a 300 μm -thick Si wafer placed at the sample position. The well established *XMAS* software (Tamura *et al.*, 2002) was used for the indexation, refinement and analysis of the Laue diffraction patterns. In Figs. 2(a) and 2(b) the Laue diffraction images collected from a 100-oriented silicon reference crystal in the low-energy reflection configuration (5–30 keV) (Hofmann *et al.*, 2009) and the present HETL configuration are shown, respectively. In the low-energy case (Fig. 2a) fewer reflections are present. They are evenly distributed over the area of the detector with the $x00$ reflection in the centre of the pattern. In the energy range

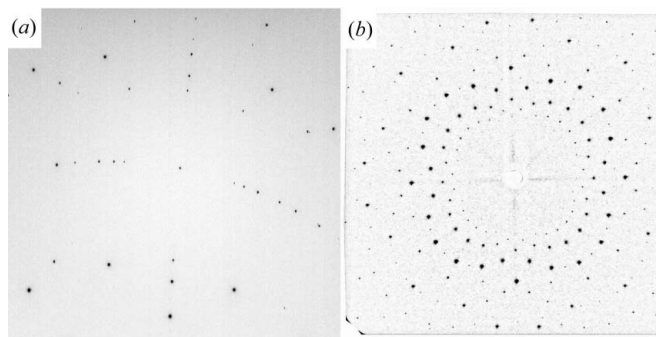


Figure 2 Silicon 100 calibration patterns. (a) Classical low-energy micro-beam Laue case. (b) High-energy transmission Laue (HETL) configuration.

from 5 to 30 keV, 49 peaks could be indexed. In the transmission set-up (Fig. 2b) a much larger number of reflections is recorded. In the centre of the pattern the shadow from the direct beamstop is visible. The central area around the beamstop is devoid of reflections. This is due to reflections at low 2θ angles occurring at high photon energies where photon flux and the efficiency of the scintillator material are reduced. Using an energy band of 50–150 keV, 250+ peaks could be indexed. The actual photon energy spectrum extends to significantly higher photon energies; however, it was found that the indexation routine became unstable beyond an upper photon energy bound of 150 keV. The larger number of reflections should bring benefits for the measurement of elastic strains, which is based on adjustment of the lattice parameters to achieve a best match of the recorded reflection positions.

As a model for the deformation of materials with FCC crystal structure, large-grained cp nickel was considered. The waisted sample shape seen in Fig. 1 was cut from a 300 μm -thick rolled material sheet and polished on both sides. It was then heat-treated in a vacuum at 1473 K for 4 h for complete re-crystallization, followed by a slow furnace cool to minimize cooling-induced residual stresses. The resulting microstructure consisted of large grains ranging from 200 μm to 1.2 mm in diameter. Most of the grains extended through the sample thickness to produce a pseudo two-dimensional micro-structure. The presence of a high number of twins is evident, a typical feature of highly annealed FCC metals (Fig. 3c). Three tensile loading increments were applied to the sample corresponding to the macroscopic elastic limit, 1.2% and 2.4% macroscopic plastic strain at the sample waist. Laue diffraction maps were collected from the central 2 mm \times 4 mm gauge region in the undeformed state and then after each deformation increment. Plotting of orientations, stresses and strains was carried out using dedicated *Matlab* scripts, as well as the *MTEX* toolbox (Hielscher & Schaeben, 2008).

3. Results and discussion

3.1. Undeformed sample

The orientation and microstructure determined by HETL measurements can be compared with both optical micrographs

and EBSD maps of lattice orientation at the sample surface. Fig. 3(a) shows a coarse HETL orientation map (100 μm point spacing) of the central region of the undeformed sample. A higher-spatial-resolution (50 μm point spacing) HETL orientation map of the 2 mm \times 4 mm gauge region is shown in Fig. 3(b). The lattice orientations in both maps agree well and the same crystallographic features (grain boundaries and twin boundaries) can be identified. The microstructure also agrees well with an optical micrograph of the gauge region (Fig. 3c). This is interesting since the HETL map corresponds to the most prominent microstructural feature through the thickness of the sample, while the optical micrograph represents an image of the sample surface. Their close agreement confirms that, to a first approximation, the sample has a pseudo two-dimensional microstructure with most grains extending through the thickness.

Fig. 3(d) shows an EBSD map of the undeformed sample gauge region measured with a 20 μm point spacing. The missing line of data was due to a microscope error. As expected, the grain morphology in the EBSD map agrees very well with the optical micrograph. It also shows generally good agreement with the fine HETL map. It is interesting to note that, while the positioning of grain boundaries is consistent in Figs. 3(b) and 3(c), twin boundaries appear shifted in some of the grains. This can be explained by observations made using focused-ion-beam (FIB) sectioning of similar samples. They

showed that while grain boundaries generally lie close to perpendicular to the sample surface, twin boundaries are often inclined (Abbey *et al.*, 2011), causing the apparent shift of twin boundaries between HETL and EBSD maps.

The lattice orientations found by HETL and EBSD agree well in most grains. However, in some locations (*e.g.* grain 1 and its twins 1a and 1b), significant differences can be seen. Similarly, the structure of grains 3, 4 and 5 that can be clearly made out in the HETL orientation map cannot be found in the EBSD map. Instead, a different grain structure is seen in their place. These differences can be attributed to microstructural variations through the sample thickness. It should also be noted in this context that the angular uncertainty associated with HETL measurements is significantly smaller ($\sim 0.005^\circ$) (Robach *et al.*, 2011) than the value achieved by commercial EBSD systems without the use of a local reference orientation ($\sim 0.1^\circ$) (Wilkinson *et al.*, 2006b). This makes Laue diffraction measurements highly suitable for the quantitative study of the subtle lattice orientation changes that occur at the onset of plastic deformation.

3.2. Orientation and stress evolution with deformation

Next, the evolution of lattice orientation and stress with the application of tensile loading to the sample is considered. Figs. 4(a) and 4(b) show, respectively, the HETL orientation

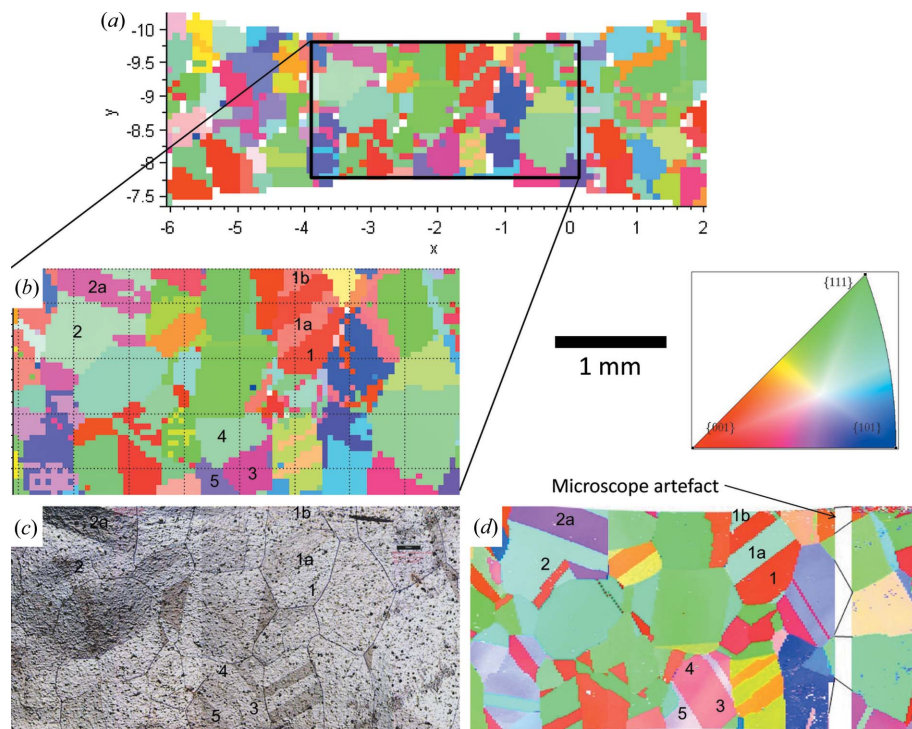


Figure 3

Illustration of the microstructure at the sample surface and in the bulk. (a) Coarse (100 μm step size) HETL orientation map of the sample central region before deformation. (b) Fine (50 μm step size) HETL orientation map of the sample gauge region before deformation. (c) Optical micrograph of the sample before deformation. (d) EBSD orientation map (20 μm step size) of the sample gauge region. The scale bar applies to (b), (c) and (d), and the same colour coding is used for all orientation maps.

maps of the undeformed sample and after 2.4% macroscopic plastic strain. The same grain structure can be reliably identified in both maps and the lattice orientations are very similar. This is expected given the comparatively modest plastic strain imposed upon the sample. The number of patterns which could not be indexed [plotted in white in Figs. 4(a) and 4(b)] increased slightly with deformation. This is due to the broadening and fragmentation of Laue spots which arises from increased lattice orientation spread within the scattering volume with increasing plastic deformation. Accurate fitting of deformed Laue peaks and the reliable determination of the reflection centres is a significant challenge.

A simple way of estimating how a given grain is likely to behave under uniaxial loading is provided by the Schmid factor, f_s . It links the critical resolved shear stress (CRSS) to the macroscopically observed yield stress (σ_y) of the crystallite, *i.e.* $\text{CRSS} = \sigma_y f_s$. For a polycrystal, f_s can be determined for each grain using a Sachs-type model which assumes the stress experienced by each crystallite is equal to the macroscopic stress state:

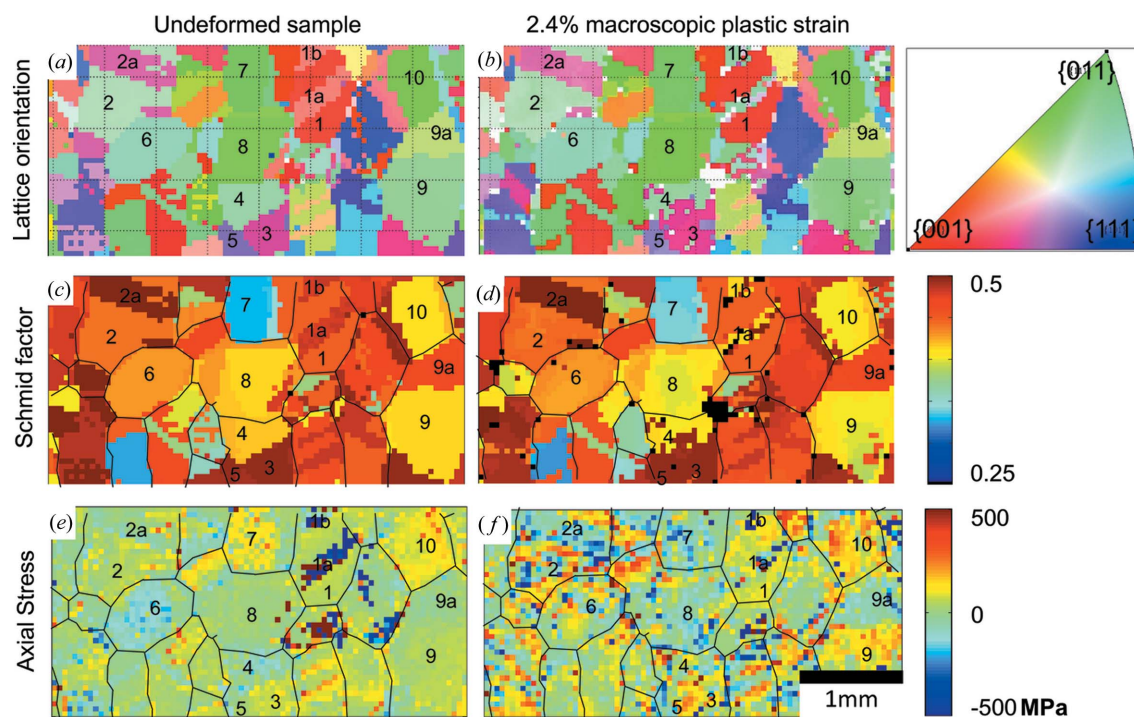


Figure 4 Evolution of orientation and strain with loading. (a) and (b) HETL orientation maps of the unloaded sample and after 2.4% plastic strain, respectively. (c) and (d) Schmid factor maps with respect to the macroscopic horizontal loading direction for the unloaded sample and after 2.4% plastic strain, respectively. (e) and (f) Axial stress (MPa) from XMAS refinement for the unloaded sample and after 2.4% plastic strain, respectively.

$$f_s = \max\left[\hat{l} \cdot \hat{n}(\hat{l} \cdot \hat{s})\right], \quad (1)$$

where \hat{l} is the macroscopic loading direction, \hat{n} the slip plane normal and \hat{s} the slip direction. This expression of f_s should be evaluated over all available slip systems: in the case of FCC nickel, four $\{111\}$ slip planes with three $\langle 110 \rangle$ slip directions each. Figs. 4(c) and 4(d) show the Schmid factor maps with respect to the horizontal macroscopic loading direction for the undeformed sample and after 2.4% plastic strain. A high Schmid factor indicates that a grain is favourably oriented for slip and should appear ‘soft’ for this loading direction, while a low Schmid factor grain should appear ‘hard’ and deform less readily. During refinement of the Laue patterns it was found that after deformation (Fig. 4d) low Schmid factor grains (e.g. grain 7) showed lower fitting errors than higher Schmid factor grains (e.g. 3, 5, 9a). This can be understood in terms of the smaller misorientations present in hard grains and hence less pronounced spreading and fragmentation of Laue spots, resulting in a better fit. This is in good agreement with low-energy Laue diffraction measurements on similar samples (Hofmann *et al.*, 2009).

Based on the elastic strains determined from XMAS refinement of the Laue patterns and the tabulated anisotropic elastic constants for single-crystalline nickel, the deviatoric stress tensor at each measurement point was determined. Figs. 4(e) and 4(f), respectively, show maps of the axial stress component (x -direction) in the unloaded sample and after 2.4% plastic deformation. A clear rise of the stress values can be seen going from the unloaded to the deformed state. A

simplistic model would suggest that, during axial plastic deformation, grains with a low Schmid factor should show higher stresses than grains with a high Schmid factor which deform more readily. This behaviour is shown by grains 9, 9a and 10 in Fig. 4. Grains 9 and 10 have a medium Schmid factor of ~ 0.4 , while twin 9a has a higher Schmid factor of ~ 0.47 . The axial stress in grains 9 and 10 is significantly higher than in twin 9a. On the other hand, grain number 7, which has a low Schmid factor, shows the opposite effect with a decrease in stress as loading is applied. This suggests that the simple Schmid model is not sufficient to understand the load sharing between multiple grains in a polycrystal.

It is important to note that care must be taken when considering the recorded stress magnitudes. In some positions they far exceed the experimentally determined macroscopic stresses which can be supported by large-grained cp nickel polycrystals (Song *et al.*, 2010). These high stress readings are likely to be spurious, especially given the high sensitivity of micro-beam Laue diffraction elastic strain measurements to geometrical perturbations and detector distortions (Robach *et al.*, 2011; Hofmann, 2011; Hofmann *et al.*, 2011). Based on the detector distortion correction and the experimental geometry, the strain accuracy in the present configuration can be estimated to be of the order of $\sim 5 \times 10^{-4}$. This is sufficient to provide qualitative information about the evolution of intragranular stresses with loading. A key assumption in this estimate is that the position of the scattering volume through the sample thickness is well known. In the case of a pseudo two-dimensional microstructure of the sample, this is a reasonable assumption as most grains extend through the thickness of the

sample. However, in the case of varying microstructure throughout the sample thickness, significant strain errors may arise as the position of the scattering volume is not known *a priori*. The magnitude of these errors can be estimated using simulation-based error analysis approaches (Hofmann *et al.*, 2011). One method of determining the positions of coherently scattering volumes (*i.e.* grains) along the beam path is to extend the well established DAXM technique (Yang *et al.*, 2004; Larson *et al.*, 2004) to higher photon energies (Hofmann *et al.*, 2012). This through-thickness resolution allows a substantial reduction of the strain errors due to the uncertainty in scattering volume position.

Lattice orientations are much more readily determined than accurate elastic strain measurements and hence form the focus of the following sections.

3.3. Misorientation after deformation

A key factor in the development and refinement of crystal plasticity simulations is the need to accurately capture the evolution of GND density. The direct link between lattice curvature and GND density was first established by Nye (1953). To visualize the variation of misorientation in the HETL measurements, a simple scheme of comparing each measurement point with its nearest neighbours can be used.

Orientation at measurement point i is captured by a rotation matrix R_i that maps from the crystal reference frame to the sample (laboratory) reference frame. The N nearest neighbours of the measurement point have rotation matrices $R_{i,n}$. The misorientation matrix $R_{\text{dif},i,n}$ between the measurement point and the n th nearest neighbour is simply given by

$$R_{\text{dif},i,n} = R_{i,n}^{-1} R_i. \quad (2)$$

Expressing $R_{\text{dif},i,n}$ in terms of the Rodriguez vector, $\hat{\omega}_{\text{dif},i,n}$, and angle, $\theta_{\text{dif},i,n}$, the local misorientation, $\theta_{\text{dif},i}$, can be defined as

$$\bar{\theta}_{\text{dif},i} = \left(\sum_{n=1}^N f_{i,n} \theta_{\text{dif},i,n} \right) / \left(\sum_{n=1}^N f_{i,n} \right). \quad (3)$$

$f_{i,n}$ is an indicator flag that is 1 if the n th neighbouring measurement point is suitable for the computation of local misorientation, and 0 if it is not. The two cases for $f_{i,n} = 0$ are when the n th neighbouring measurement position could not be indexed or when $\theta_{\text{dif},i,n}$ is greater than a certain threshold θ_{thr} . By carefully choosing θ_{thr} one can distinguish between the small misorientations which occur within grains during plastic deformation and the large orientation changes found when crossing a grain boundary. It is not possible to compute $\bar{\theta}_{\text{dif},i}$ when the reference point has no eligible nearest neighbours (*i.e.* $\sum_{n=1}^N f_{i,n} = 0$), or if the Laue pattern at the reference position could not be indexed (*i.e.* R_i is not available). These positions are plotted in black in Fig. 5.

Fig. 5 shows a map of $\bar{\theta}_{\text{dif},i}$ after the last load increment (2.4% macroscopic plastic strain). The acceptance threshold was set to $\theta_{\text{thr}} = 4^\circ$, sufficiently large to include any intra-granular rotations, while discriminating against orientations of neighbouring grains. The presence of a number of bands with high misorientation is evident. The direction of these bands

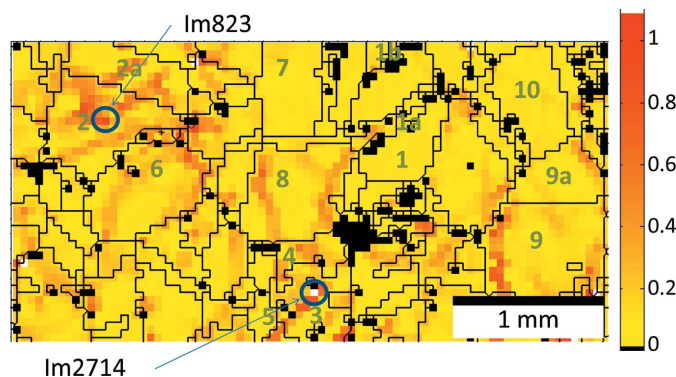


Figure 5

Plot of local average misorientation $\bar{\theta}_{\text{dif},i}$ after the last deformation increment (2.4% macroscopic plastic strain). The colour bar shows misorientation in degrees. Two measurement points of particularly high misorientation are highlighted. In grain 2 this corresponds to diffraction pattern Im823 and in grain 3 to pattern Im2714.

varies from being almost perpendicular to the macroscopic loading direction (grain 8) to forming an angle of $\sim 30^\circ$ (grain 2). Interestingly, the presence of high lattice misorientation does not seem to be confined to high Schmid factor grains [Figs. 4(c) and 4(d)]. Grain 7, with a low Schmid factor, shows only little intra-granular misorientation, which is consistent with the sharp Laue peaks observed from this grain after deformation. Grains 8 and 9 have a medium Schmid factor of 0.41. Both show significantly higher degrees of lattice misorientation than the higher Schmid factor twin 9a. This suggests that the formation of high local orientation gradients not only depends on lattice orientation, but also importantly on the local grain neighbourhood (Mika & Dawson, 1998; Tamura *et al.*, 2003). We also note that bands of high misorientation can be readily transmitted across twin boundaries (grain 2 and its twin 2a) and, to a lesser extent, across grain boundaries (grains 2 and 6).

Intra-granular misorientation is also reflected by the streaking and fragmentation of Laue peaks owing to orientation spread within the scattering volume at each measurement point. In the misorientation map in Fig. 5, two positions with particularly high values of $\bar{\theta}_{\text{dif},i} > 1^\circ$ were selected (circled in blue). They correspond to diffraction images Im823 and Im2714 in grains 2 and 3, respectively.

Diffraction image Im823 is shown in Fig. 6(a). The Laue reflections show a dumbbell-type structure, consisting of two intense spots linked by a weaker streak oriented approximately in the radial direction. A further contribution to Laue spot streaking, apart from that due to GND-induced lattice orientation spread, is the elongation in the radial direction owing to the length of the scattering volume along the incident beam. In a perfect strain-free crystal, each Laue spot would be a white-beam topograph of the illuminated coherently scattering volume, *i.e.* a projection of the coherently scattering volume onto the detector at the corresponding 2θ angle. The length, l_m , of each Laue spot, assuming a scattering volume with length L along the incident beam direction and small height and width, would be

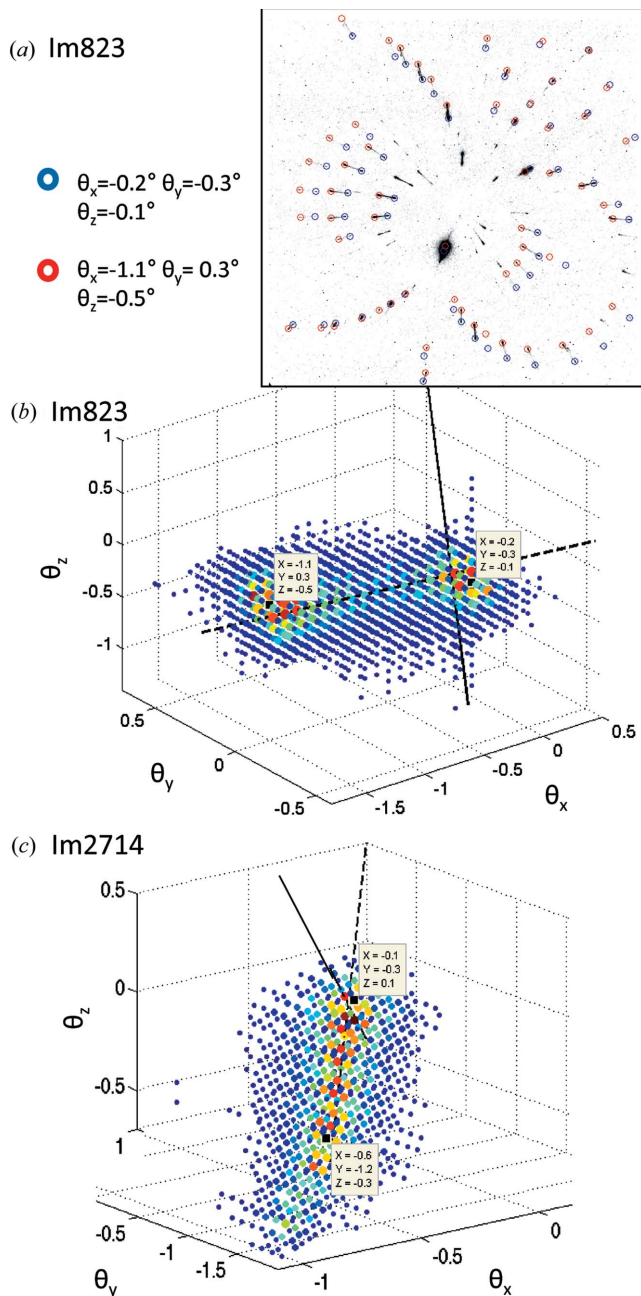


Figure 6 Illustration of the misorientation spread in the scattering volume at positions Im823 and Im2714 after the last deformation increment. (a) Experimentally collected Laue diffraction pattern Im823 with superimposed predicted reflection positions. (b) Four-dimensional orientation plot of Im823. Small rotation angles θ_x , θ_y and θ_z are given in degrees. Superimposed are the predicted rotation axes for the highest Schmid factor slip system $(\bar{1}\bar{1}1)[110]$ (solid line) and for the $(\bar{1}\bar{1}1)[01\bar{1}]$ slip system (dashed line). (c) Four-dimensional orientation plot of Im2714. Superimposed are the predicted rotation axes for the two highest Schmid factor slip systems: $(111)[\bar{1}0\bar{1}]$ (solid line) and $(\bar{1}\bar{1}1)[\bar{1}01]$ (dashed line).

$$l_m = L \tan(2\theta). \quad (4)$$

In Fig. 6(a) the streaking of reflections is clearly not only a function of their 2θ position but also of their χ position on the detector. This means that the streaking at least in part is due to GND-induced orientation spread within the scattering

volume. In fact, based on the experimental geometry and sample thickness, the GND-induced orientation spread that would cause streaking of the same magnitude as the sampling volume length effect can be estimated as $\sim 0.05^\circ$. This is substantially smaller than the orientation spread present in image Im823 which is of the order of $\sim 1^\circ$ as explained below. Hence the streaking of reflections in image Im823 is dominated by GND-induced lattice orientation spread in the scattering volume.

One approach to separating the effects of GND-induced streaking and scattering volume length streaking is to notice that the former increases linearly with distance, whilst the latter remains constant. By fitting Laue spots at different sample-to-detector distances their contributions could be separated. Alternatively techniques could be employed that provide resolution of lattice orientation distribution along the incident beam direction as discussed elsewhere (Hofmann *et al.*, 2012).

To quantify the orientation spread within the scattering volume of a given Laue pattern, a template-matching scheme based on a previously proposed analysis routine for classical micro-beam Laue diffraction was used (Gupta & Agnew, 2009). The idea is to generate Laue patterns with lattice orientations which deviate slightly from the average orientation of the scattering volume and then assess how well they match the experimental Laue pattern. By generating the slight angular variations on a regular grid, a picture of the orientation spread within the scattering volume in terms of three misorientation angles can be built up.

In the HETL configuration the mean lattice orientation of each Laue pattern, R_i , is found by XMAS indexation and refinement. Added to this are small rotations θ_x , θ_y and θ_z about the x , y and z crystal axes, respectively, which are applied *before* rotation R_i . Expressing these rotations as Rodriguez vectors, one can use the fact that, for small rotations, Rodriguez vectors are additive. Hence, the total Rodriguez vector owing to θ_x , θ_y and θ_z is $\hat{\omega}_{xyz} \simeq (\theta_x, \theta_y, \theta_z)/|(\theta_x, \theta_y, \theta_z)|$ and the associated Rodriguez angle, θ_{xyz} , is $\theta_{xyz} \simeq |(\theta_x, \theta_y, \theta_z)|$. Using $\hat{\omega}_{xyz}$ and θ_{xyz} , the rotation matrix R_{xyz} capturing reorientation owing to the small rotations θ_x , θ_y and θ_z can be determined. The overall orientation matrix, R , is then

$$R = R_i R_{xyz}. \quad (5)$$

Based on R , ray tracing was used to find the predicted Laue spot positions, P , in detector pixel coordinates. Next, a correlation coefficient C was defined as

$$C(\theta_x, \theta_y, \theta_z) = \sum I(P). \quad (6)$$

The sum was taken over all reflections for which the forward prediction was carried out. $I(P)$ is the intensity value of the pixel at position P in the Laue image. The correlation coefficient was evaluated over a range of θ_x , θ_y and θ_z angles from -3° to $+3^\circ$ in increments of 0.1° .

Initially the scheme was applied to background-subtracted Laue images. However, it was found that the correlation coefficient in this case was dominated by a small number of

high-intensity peaks which were well matched, even if the majority of lower-intensity peaks were not well matched. Gupta & Agnew (2009) avoided this difficulty by binarising the images, setting pixels within a reflection to 1 and outside to 0. To retain more of the reflection details, we introduced instead an arbitrary reflection intensity cut-off of 50 counts.

The dumbbell structure of the experimental Laue spots in image Im823 (Fig. 6*a*) is clearly captured in the four-dimensional plot of C versus θ_x , θ_y and θ_z in Fig. 6*b*). The colour coding reflects the magnitude of $C(\theta_x, \theta_y, \theta_z)$. Two maxima of the correlation coefficient exist, one at $\theta_x = -0.2^\circ$, $\theta_y = -0.3^\circ$ and $\theta_z = -0.1^\circ$ and the other at $\theta_x = -1.1^\circ$, $\theta_y = 0.3^\circ$ and $\theta_z = -0.5^\circ$. In Fig. 6*a*) the predicted Laue spot positions for these two maxima are shown superimposed on the experimental Laue pattern Im823 in blue and red, respectively. As expected, they lie on the two intense spots at either end of the experimental Laue streaks, confirming the correctness of the four-dimensional orientation plot.

The angular separation between the two correlation coefficient maxima is $\sim 1.2^\circ$ and corresponds to a rotation about the $[-0.9, 0.6, -0.4]$ crystal axis, which can be approximated as $[\bar{2}1\bar{1}]$ [dashed line in Fig. 6*b*]). To estimate the lattice rotations arising from activity of a given slip system, one can assume that the GND distribution that is introduced is dominated by edge dislocations on that slip system (Barabash *et al.*, 2003, 2004*a*). The expected lattice rotation axis can be found by taking the cross product of the slip plane normal, \hat{n} , and the slip direction, \hat{s} . The observed streaking with rotation about the $[\bar{2}1\bar{1}]$ axis thus corresponds to an active slip system with plane normal $\hat{n} = (\bar{1}\bar{1}1)$ and slip direction $\hat{s} = [0\bar{1}\bar{1}]$. Given the macroscopic $[100]$ loading direction (laboratory coordinates), the Schmid factor for this slip system is 0.33. However, this is only the second largest Schmid factor slip system. The highest Schmid factor of 0.436 is achieved for the same slip plane normal $\hat{n} = (\bar{1}\bar{1}1)$ and the $\hat{s} = [\bar{1}10]$ slip direction. The expected lattice rotation axis owing to GNDs in this case is the $[112]$ axis [solid line in Fig. 6*b*]). This clearly does not agree with the orientation of the greatest correlation factor cloud.

A similar analysis of orientation spread in the scattering volume was performed for Im2714. The four-dimensional orientation plot (Fig. 6*c*) shows an elongated cloud with a central core/streak of high correlation coefficient. It corresponds to an orientation range of $\sim 1.1^\circ$ about the $[0.5, 0.9, 0.4]$ crystal axis, which can be approximated as $[121]$. From the mean lattice orientation found by *XMAS* indexation, one can see that, with respect to the macroscopic loading direction, grain 3 at Im2714 is actually oriented for double slip. It has two slip systems with equally high Schmid factors of 0.492: $(\bar{1}\bar{1}1)[\bar{1}0\bar{1}]$ and $(\bar{1}\bar{1}1)[\bar{1}0\bar{1}]$. Slip on the former would cause lattice rotations about the $[121]$ crystal axis [dashed line in Fig. 6*c*]), while the latter would cause rotations about the $[\bar{1}2\bar{1}]$ crystal axis [solid line in Fig. 6*c*]). The orientation cloud is clearly aligned with the dashed line, suggesting the increased presence of GNDs on the $(\bar{1}\bar{1}1)[\bar{1}0\bar{1}]$ slip system, and hence that this is the primary active slip system. No spreading of the reflections occurs along the solid line; the $(\bar{1}\bar{1}1)[\bar{1}0\bar{1}]$ slip system was not active.

The deformation behaviour of grains 2 and 3 raises some interesting questions. Why was only the second highest Schmid factor slip system active in grain 2, while the one with the highest Schmid factor was inactive? How is the active slip system selected from the two which have the same Schmid factor in grain number 3? In both grains, just considering the loading applied remotely, as is the case of simple Schmid factor analysis, clearly does not fully capture the local deformation response. Rather, the active deformation mechanism is dependent on the local loading conditions, which are substantially different from the macroscopically applied loading. The reasons for this are the anisotropic elastic–plastic properties of the constituent grains and the infinite number of possibilities in which the local microstructure can be assembled. In fact, the variation of loading experienced by individual grains owing to the constraining effects of their neighbours, the so-called neighbourhood effect, is well documented in computational studies of polycrystalline deformation (Barbe *et al.*, 2001*a,b*, 2003; Diard *et al.*, 2005). This can also be considered in the context of the so-called ‘localization’ tensors that purport to provide generic relationships between ‘global’ remotely applied stresses and ‘local’ stress states experienced by individual grains and sub-grain regions. Various approaches to the introduction of such tensors have been advanced for polycrystal elasticity (Eshelby, 1957, 1959; Kröner, 1958), polycrystal plasticity (Hill, 1950, 1965; Braccini & Wilkinson, 2003) and fatigue analysis (Dang-Van, 1993).

The current data set is eminently suitable to provide a direct validation of crystal elasto-plasticity simulation codes and to test their ability to accurately capture heterogeneous grain-level deformation behaviour, active slip system selection, *etc.* In the low-energy case, initial studies of this kind have been reported with good success (Ohashi *et al.*, 2009; Song *et al.*, 2010). Use of transmission measurements offers the important advantage that the entire sample thickness is probed, removing the ambiguity about sampling volume size which can exist in low-energy measurements. Modelling efforts to this end are under way and will be reported at a later stage.

The evolution of GND density in the sample could be determined considering the variations in lattice curvature. In fact, it could be evaluated either by considering the changes in orientation between adjacent measurement points, or considering the orientation spread present *within* the gauge volume at each measurement point. The HETL diffraction data set is essentially two-dimensional owing to the lack of spatial resolution through the sample thickness. This means that only three of the six components of the Nye tensor could be found (Sun *et al.*, 2000). Using the orientation spread in the scattering volume (Fig. 6), an estimate of the GND density, ρ_{GND} , on the active slip system could be made using the simple relation

$$\rho_{\text{GND}} = \hat{\alpha}_{\text{GND}}/Lb, \quad (7)$$

where $\hat{\alpha}_{\text{GND}}$ is the angular lattice orientation change in radians, L is the side length of the considered volume and b is the burgers vector. This raises the interesting question of which dimension L should be used for the computation, given

that the gauge volume has a high aspect ratio of 12:1 (incident beam size of $25\ \mu\text{m} \times 25\ \mu\text{m}$, sample thickness of $300\ \mu\text{m}$). If misorientation occurred primarily perpendicular to the incident beam, the required dislocation density would be 12 times higher than if misorientation occurred primarily through the sample thickness. To overcome these uncertainties, it is essential that HETL diffraction is extended to allow three-dimensional resolution of lattice orientation and strain through the sample thickness.

During recent experiments at the high-energy beamline I12 at the Diamond Light Source (DLS), two avenues for further development in this direction have been explored. One option is to extend the existing DAXM technique to higher photon energies. This allows the reconstruction of depth-resolved Laue patterns and combines the increased penetration of HETL with three-dimensional grain-level characterization of lattice orientation and elastic strain in thick samples. Alternatively, tomographic reconstruction principles can be used to determine lattice orientation and elastic strain in three dimensions based on grain-specific scattered intensity from Laue patterns recorded at different sample orientations. Both techniques have yielded promising first results that will be reported in detail in the near future.

4. Conclusions

This paper presents a detailed description of the first HETL micro-beam X-ray diffraction study. The new technique was used to investigate the behaviour of a polycrystalline large-grained $300\ \mu\text{m}$ -thick Ni sheet sample during *in situ* tensile deformation. A number of key points can be noted about the method:

(i) HETL measurements were successfully performed to study the deformation response within individual grains of a thicker polycrystalline nickel sample.

(ii) Careful calibration and detector distortion correction were essential for the successful analysis of HETL diffraction patterns.

(iii) Analysis of the experimental data could be carried out using well-established micro-beam Laue diffraction tools such as the *XMAS* software package (Tamura *et al.*, 2002) and the *MTEX* toolbox for orientation plotting (Hielscher & Schaeben, 2008).

(iv) Lattice orientation was successfully mapped and followed during deformation. Agreement with EBSD surface maps was very good. While qualitative information about lattice strains could be found, experimental errors were too high for quantitative measurements.

A significant reduction of the experimental errors could be achieved by using a detector with lower distortion and a larger pixel matrix, placed further away from the sample. This would improve the accuracy with which reflection positions in reciprocal space can be found and reduce the sensitivity of the technique to sample positioning uncertainties. The development of techniques providing three-dimensional resolution in HETL measurements opens up exciting possibilities for the

grain-level characterization of real engineering components and is being actively pursued in our group.

Grains in the large-grained nickel sample only experienced comparatively small lattice rotations as a result of the imposed plastic deformation. Within individual crystallites, clear heterogeneities of lattice orientation could be observed after the last deformation increment. After 2.4% plastic strain, we found bands of increased lattice misorientation that formed angles of $\sim 90^\circ$ to $\sim 30^\circ$ with the macroscopic loading direction. Transmission of these bands occurred across twin boundaries and less readily across grain boundaries. Their presence was not limited to high Schmid factor grains. Using a pattern-matching approach we explored misorientation within the scattering volume and determined the angular spread as well as the active slip system. Based on the study of multiple points in the sample, we found that behaviour differed significantly from the simple Schmid factor model. This was ascribed to the strong dependence of local deformation response on both the initial lattice orientation and the local grain neighbourhood. To elucidate behaviour at this scale, a comparison with detailed crystal plasticity simulations should be made, providing an extension to previous investigations (Ohashi *et al.*, 2009; Song *et al.*, 2010). The present data set is ideally suited to this purpose and efforts to this end are currently under way.

We would like to thank Dr Matthew Peel, Dr John Daniels and Dr Leigh Connor for their contributions to the experimental aspects of this paper, and Professor Olivier Castelnau for many helpful suggestions. Financial support provided by the EPSRC in the form of a DTA and a PhD+ grant, as well as project grants EP/H003215, EP/G035059 and EP/I020691 is gratefully acknowledged. We also very much appreciate the allocation of beam time on the ID15 instrument at the ESRF and on the I12 beamline at the DLS.

References

- Abbey, B., Hofmann, F., Belnoue, J., Rack, A., Tucoulou, R., Hughes, G., Eve, S. & Korsunsky, A. M. (2011). *Scr. Mater.* **64**, 884–887.
- Aifantis, E. C. (1987). *Int. J. Plast.* **3**, 211–247.
- Arsenlis, A., Cai, W., Tang, M., Rhee, M., Opperstrup, T., Hommes, G., Pierce, T. G. & Bulatov, V. V. (2007). *Modell. Simul. Mater. Sci. Eng.* **15**, 553–596.
- Arsenlis, A. & Parks, D. M. (2002). *J. Mech. Phys. Solids*, **50**, 1979–2009.
- Ashby, M. F. (1970). *Philos. Mag.* **21**, 399–424.
- Barabash, O. M., Horton, J. A., Babu, S. S., Vitek, J. M., David, S. A., Park, J. W., Ice, G. E. & Barabash, R. I. (2004a). *J. Appl. Phys.* **96**, 3673–3679.
- Barabash, R., Barabash, O. M., Ice, G. E., David, S. A., Feng, Z. & Horton, J. A. Jr (2007). *Rev. Adv. Mater. Sci.* **15**, 49–55.
- Barabash, R., Ice, G. E., Larson, B. C., Pharr, G. M., Chung, K. S. & Yang, W. (2001). *Appl. Phys. Lett.* **79**, 749–751.
- Barabash, R. I., Ice, G. E. & Pang, J. W. L. (2005). *Mater. Sci. Eng. A*, **400–401**, 125–131.
- Barabash, R. I., Ice, G. E., Tamura, N., Valek, B. C., Bravman, J. C., Spolenak, R. & Patel, J. R. (2004b). *Microelectron. Eng.* **75**, 24–30.

- Barabash, R. I., Ice, G. E. & Walker, F. J. (2003). *J. Appl. Phys.* **93**, 1457–1464.
- Barbe, F., Decker, L., Jeulin, D. & Cailletaud, G. (2001a). *Intl J. Plast.* **17**, 513–536.
- Barbe, F., Forest, S. & Cailletaud, G. (2001b). *Intl J. Plast.* **17**, 537–563.
- Barbe, F., Forest, S., Quilici, S. & Cailletaud, G. (2003). *Rev. Met. Paris*, **100**, 815–823.
- Beaudoin, A. J., Acharya, A., Chen, S. R., Korzekwa, D. A. & Stout, M. G. (2000). *Acta Mater.* **48**, 3409–3423.
- Bei, H., Barabash, R. I., Ice, G. E., Liu, W., Tischler, J. & George, E. P. (2008). *Appl. Phys. Lett.* **93**, 071904.
- Braccini, M. & Wilkinson, D. S. (2003). *Scr. Mater.* **49**, 53–57.
- Budai, J. D., Yang, W., Tamura, N., Chung, J. S., Tischler, J. Z., Larson, B. C., Ice, G. E., Park, C. & Norton, D. P. (2003). *Nat. Mater.* **2**, 487–492.
- Bulatov, V. V. & Cai, W. (2006). *Computer Simulations of Dislocations*. Oxford University Press.
- Bulatov, V. V., Hsiung, L. L., Tang, M., Arsenlis, A., Bartelt, M. C., Cai, W., Florando, J. N., Hiratani, M., Rhee, M., Hommes, G., Pierce, T. G. & de la Rubia, T. D. (2006). *Nature (London)*, **440**, 1174–1178.
- Busso, E. P., Meissonnier, F. T. & O'Dowd, N. P. (2000). *J. Mech. Phys. Solids*, **48**, 2333–2361.
- Cheng, S., Stoica, A. D., Wang, X. L., Ren, Y., Almer, J., Horton, J. A., Liu, C. T., Clausen, B., Brown, D. W., Liaw, P. K. & Zuo, L. (2009). *Phys. Rev. Lett.* **103**, 035502.
- Cheong, K. S., Busso, E. P. & Arsenlis, A. (2005). *Intl J. Plast.* **21**, 1797–1814.
- Choi, W. J., Lee, T. Y., Tu, K. N., Tamura, N., Celestre, R. S., MacDowell, A. A., Bong, Y. Y. & Nguyen, L. (2003). *Acta Mater.* **51**, 6253–6261.
- Crisfield, M. A. (1991). *Non-Linear Finite Element Analysis of Solids and Structures: Essentials*. New York: Wiley.
- Dang-Van, K. (1993). *ASTM Spec. Tech. Publ.* **1191**, 120.
- Deshpande, V. S., Needleman, A. & Van der Giessen, E. (2003). *Acta Mater.* **51**, 1–15.
- Diard, O., Leclercq, S., Rousselier, G. & Cailletaud, G. (2005). *Intl J. Plast.* **21**, 691–722.
- Dunne, F. & Petrinic, N. (2005). *Introduction to Computational Plasticity*. Oxford University Press.
- Dunne, F. P. E., Wilkinson, A. J. & Allen, R. (2007). *Intl J. Plast.* **23**, 273–295.
- Eshelby, J. D. (1957). *Proc. R. Soc. London Ser. A*, **241**, 376–396.
- Eshelby, J. D. (1959). *Proc. R. Soc. London Ser. A*, **252**, 561–569.
- Fleck, N. A. & Hutchinson, J. W. (2001). *J. Mech. Phys. Solids*, **49**, 2245–2271.
- Fleck, N. A., Muller, G. M., Ashby, M. F. & Hutchinson, J. W. (1994). *Acta Metall. Mater.* **42**, 475.
- Fu, X., Poulsen, H. F., Schmidt, S., Nielsen, S. F., Lauridsen, E. M. & Juul Jensen, D. (2003). *Scr. Mater.* **49**, 1093–1096.
- Gloaguen, D., Berchi, T., Girard, E. & Guilln, R. (2007). *Acta Mater.* **55**, 4369–4379.
- Gupta, V. K. & Agnew, S. R. (2009). *J. Appl. Cryst.* **42**, 116–124.
- Hall, A. E. O. (1951). *Proc. Phys. Soc. B*, **9**, 747.
- Hielscher, R. & Schaeben, H. (2008). *J. Appl. Cryst.* **41**, 1024–1037.
- Hill, R. (1950). *The Mathematical Theory of Plasticity*. Oxford: Clarendon Press.
- Hill, R. (1965). *J. Mech. Phys. Solids*, **13**, 89–101.
- Hofmann, F. (2011). PhD thesis, University of Oxford, UK.
- Hofmann, F., Abbey, B., Connor, L., Baimpas, N., Song, X., Keegan, S. & Korsunsky, A. M. (2012). *Intl J. Mater. Res.* **103**, 192–199.
- Hofmann, F., Eve, S., Belnoue, J. P., Micha, J.-S. & Korsunsky, A. M. (2011). *Nucl. Instrum. Methods Phys. Res. A*, **660**, 130–137.
- Hofmann, F., Song, X., Dolbnya, I., Abbey, B. & Korsunsky, A. M. (2009). *Proc. Eng.* **1**, 193–196.
- Hofmann, F., Song, X., Jun, T. S., Abbey, B., Peel, M., Daniels, J., Honkimäki, V. & Korsunsky, A. M. (2010). *Mater. Lett.* **64**, 1302–1305.
- Ice, G. E., Larson, B. C., Yang, W., Budai, J. D., Tischler, J. Z., Pang, J. W. L., Barabash, R. I. & Liu, W. (2005). *J. Synchrotron Rad.* **12**, 155–162.
- Johnson, G., King, A., Honnicke, M. G., Marrow, J. & Ludwig, W. (2008). *J. Appl. Cryst.* **41**, 310–318.
- King, A., Herbig, M., Ludwig, W., Reischig, P., Lauridsen, E. M., Marrow, T. & Buffire, J. Y. (2010). *Nucl. Instrum. Methods Phys. Res. B*, **268**, 291–296.
- King, A., Johnson, G., Engelberg, D., Ludwig, W. & Marrow, J. (2008). *Science*, **321**, 382–385.
- Korsunsky, A. M., Collins, S. P., Owen, R. A., Daymond, M. R., Achtioui, S. & James, K. E. (2002). *J. Synchrotron Rad.* **9**, 77–81.
- Korsunsky, A. M., Song, X., Hofmann, F., Abbey, B., Xie, M., Connolley, T., Reinhard, C., Atwood, R. C., Connor, L. & Drakopoulos, M. (2010). *Mater. Lett.* **64**, 1724–1727.
- Kröner, E. (1958). *Z. Phys. A*, **151**, 504–518.
- Larson, B. C., Yang, W., Ice, G. E., Budai, J. D. & Tischler, J. Z. (2002). *Nature (London)*, **415**, 887–890.
- Larson, B. C., Yang, W., Tischler, J. Z., Ice, G. E., Budai, J. D., Liu, W. & Weiland, H. (2004). *Intl J. Plast.* **20**, 543–560.
- Lemaitre, J., Chaboche, J.-L. & Shrivastava, B. (1994). *Mechanics of Solid Materials*. Cambridge University Press.
- Lloyd, D. J. (1994). *Intl Mater. Rev.* **39**, 1–23.
- Ludwig, W., Reischig, P., King, A., Herbig, M., Lauridsen, E. M., Johnson, G., Marrow, T. J. & Buffière, J. Y. (2009). *Rev. Sci. Instrum.* **80**, 033905.
- Ludwig, W., Schmidt, S., Lauridsen, E. M. & Poulsen, H. F. (2008). *J. Appl. Cryst.* **41**, 302–309.
- Maass, R., Van Petegem, S., Grolimund, D., Van Swygenhoven, H., Kiener, D. & Dehm, G. (2008a). *Appl. Phys. Lett.* **92**, 071905.
- Maass, R., Van Petegem, S., Zimmermann, J., Borca, C. N. & Van Swygenhoven, H. (2008b). *Scr. Mater.* **59**, 471–474.
- McElhaney, K. W., Vlassak, J. J. & Nix, W. D. (1998). *J. Mater. Res.* **13**, 1300–1306.
- Meissonnier, F. T., Busso, E. P. & O'Dowd, N. P. (2001). *Intl J. Plast.* **17**, 601–640.
- Mika, D. P. & Dawson, P. R. (1998). *Mater. Sci. Eng. A*, **257**, 62–76.
- Mimura, H., Handa, S., Kimura, T., Yumoto, H., Yamakawa, D., Yokoyama, H., Matsuyama, S., Inagaki, K., Yamamura, K., Sano, Y., Tamasaku, K., Nishino, Y., Yabashi, M., Ishikawa, T. & Yamauchi, K. (2010). *Nat. Phys.* **6**, 122–125.
- Nielsen, S. F., Lauridsen, E. M., Juul Jensen, D. & Poulsen, H. F. (2001). *Mater. Sci. Eng. A*, **319–321**, 179–181.
- Nye, J. F. (1953). *Acta Metall.* **1**, 153–162.
- Ohashi, T., Barabash, R. I., Pang, J. W. L., Ice, G. E. & Barabash, R. I. (2009). *Intl J. Plast.* **25**, 920–941.
- Petch, N. J. (1953). *J. Iron Steel Inst.* **174**, 25–28.
- Poulsen, H. F., Nielsen, S. F., Lauridsen, E. M., Schmidt, S., Suter, R. M., Lienert, U., Margulies, L., Lorentzen, T. & Juul Jensen, D. (2001). *J. Appl. Cryst.* **34**, 751–756.
- Robach, O., Micha, J.-S., Ulrich, O. & Gergaud, P. (2011). *J. Appl. Cryst.* **44**, 688–696.
- Song, X., Hofmann, F. & Korsunsky, A. M. (2010). *Philos. Mag.* **90**, 3999–4011.
- Song, X., Zhang, S. Y., Dini, D. & Korsunsky, A. M. (2008a). *Comput. Mater. Sci.* **44**, 131–137.
- Song, X., Zhang, S. Y., Dini, D. & Korsunsky, A. M. (2008b). *Mater. Sci. Forum*, **571–572**, 271–276.
- Spolenak, R., Brown, W. L., Tamura, N., MacDowell, A. A., Celestre, R. S., Padmore, H. A., Valek, B., Bravman, J. C., Marieb, T., Fujimoto, H., Batterman, B. W. & Patel, J. R. (2003). *Phys. Rev. Lett.* **90**, 096102.
- Steuwer, A., Santisteban, J. R., Turski, M., Withers, P. J. & Buslaps, T. (2005). *Nucl. Instrum. Methods Phys. Res. B*, **238**, 200–204.
- Sun, S., Adams, B. L. & King, W. E. (2000). *Philos. Mag. A*, **80**, 9–25.
- Tamura, N., Celestre, R. S., MacDowell, A. A., Padmore, H. A., Spolenak, R., Valek, B. C., Chang, N. M., Manceau, A. & Patel, J. R. (2002). *Rev. Sci. Instrum.* **73**, 1369–1372.

- Tamura, N., MacDowell, A. A., Spolenak, R., Valek, B. C., Bravman, J. C., Brown, W. L., Celestre, R. S., Padmore, H. A., Batterman, B. W. & Patel, J. R. (2003). *J. Synchrotron Rad.* **10**, 137–143.
- Van der Giessen, E. & Needleman, A. (1995). *Modell. Simul. Mater. Sci. Eng.* **3**, 689–735.
- Wanner, A. & Dunand, D. (2000). *Metall. Mater. Trans. A*, **31**, 2949–2962.
- Wilkinson, A. J., Meaden, G. & Dingley, D. J. (2006a). *Ultramicroscopy*, **106**, 307–313.
- Wilkinson, A. J., Meaden, G. & Dingley, D. J. (2006b). *Mater. Sci. Technol.* **22**, 1271–1278.
- Yan, H. & Noyan, I. C. (2005). *J. Appl. Phys.* **98**, 073527.
- Yang, W., Larson, B. C., Tischler, J. Z., Ice, G. E., Budai, J. D. & Liu, W. (2004). *Micron*, **35**, 431–439.